Solar RRL
www.solar-rrl.com

A Facile Low Prevacuum Treatment to Enhance the Durability of Nonfullerene Organic Solar Cells

*Mohamed Samir, Angel Sacramento, Osbel Almora, Josep Pallarès, and Lluis F. Marsal**

Herein, a straightforward vacuum-assisted method is introduced to enhance the stability of nonfullerene organic solar cells (OSCs). The method, termed "prevacuum" involves subjecting the active layer (D18:Y6) to a low-pressure vacuum (−1 bar) before thermal annealing at 100 °C. Compared to untreated devices, prevacuum-treated OSCs exhibit a notable increase in power conversion efficiency from 13.71% to 14.90%. This enhancement is attributed to improved light absorption and charge extraction, as evidenced by external quantum efficiency measurements. Moreover, prevacuum treatment significantly improves device stability under operational conditions, with a 30% power loss occurring after 8.25 h compared to 4.5 h for untreated devices. This improvement is attributed to the removal of volatile components and impurities during the vacuum process, leading to a more hydrophobic and stable active layer. The study demonstrates the efficacy of prevacuum treatment as a simple and accessible method for enhancing the performance and longevity of OSCs, paving the way for their broader application in sustainable energy technologies.

1. Introduction

Organic solar cells (OSCs) have emerged as a promising photovoltaic technology due to their potential for low-cost, flexible, and lightweight solar energy conversion.[1–3] In recent years, the efficiency of single-junction devices has exceeded 19% and 20%,[4–6] narrowing the gap with perovskite and silicon solar cells.[1] This progress is largely attributed to the development of nonfullerene acceptors (NFAs), particularly those with A–D–A architectures like ITIC and Y6.[3,7,8] These NFAs offer advantages over fullerene-based acceptors, including tunable absorption ranges, enhanced intramolecular charge transfer, and improved molecular packing orientations. The design of novel small-molecule donors and polymer donors, coupled with advancements in morphology control techniques such as ternary blending and post-treatment methods, has further contributed to the enhanced performance of OSCs. The exploration of alternative device architectures, including semitransparent and tandem structures, has also expanded the potential applications of OSCs.[1,7–12]

While high efficiency is crucial for OSC commercialization, achieving long-term stability remains a major challenge. Recent research has led to the development of intrinsically stable OSCs with extrapolated T80 lifetimes reaching impressive durations, like $4.9 \times 10\hat{}7$ h. The incorporation of protective layers, such as UV-resistant coatings, has also contributed to enhancing the operational lifetime of NFA-based OSCs, with predicted lifetimes exceeding 50 000 h.[13,14] These breakthroughs highlight the growing potential of OSCs for long-term, practical applications.

Fullerene derivatives, such as [6,6]-phenyl-C61-butyric acid methyl ester, dominated the OSC field for over two decades due to their favorable properties like high electron mobility and ease of processing.[2,15] However, their limitations, including weak light absorption and large energy losses, hindered further efficiency improvements.[2,15,16] The emergence of NFAs, with their tunable energy levels, strong absorption, and improved charge transport, has revolutionized OSC research.[2,3,7,15] The collaborative development of novel donor and acceptor materials, along with a deeper understanding of device physics, has led to significant breakthroughs in OSC performance, paving the way for potential commercial applications.[3,7,17,18]

The bulk-heterojunction (BHJ) architecture, where donor and acceptor materials are intermixed, has been a cornerstone in OSC development.[19,20] This architecture maximizes the interfacial area between donor and acceptor materials, facilitating exciton dissociation and charge generation. However, BHJ morphology control remains a challenge, as it significantly impacts charge transport and recombination processes.[19,21] Recent studies have explored novel donor–acceptor combinations, such as D18:Y6, and innovative processing techniques

M. Samir, O. Almora, J. Pallarès, L. F. Marsal
Department of Electronic, Electric and Automatic Engineering
Universitat Rovira i Virgili
43007 Tarragona, Spain
E-mail: lluis.marsal@urv.cat

A. Sacramento
Department of Electrical Engineering
Center for Research and Advanced Studies of National Polytechnic Institute
Mexico City 07360, Mexico

The ORCID identification number(s) for the author(s) of this article can be found under https://doi.org/10.1002/solr.202400479.

DOI: 10.1002/solr.202400479

to optimize BHJ morphology and enhance device performance.[22–24] Despite these advancements, challenges like controlling phase separation and achieving optimal domain sizes persist in BHJ OSCs.[19,23]

Posttreatment processes, such as solvent vapor annealing (SVA) and thermal annealing (TA), are crucial for optimizing the morphology and performance of BHJ OSCs.[25–27] SVA, involving exposure to solvent vapors, can induce molecular rearrangement, leading to improved phase separation and molecular packing.[25,27,28] However, excessive SVA can lead to detrimental effects on device performance and stability.[28,29] TA, on the other hand, can enhance crystallinity and charge transport but may also cause material degradation if not carefully controlled.[26,29,30] Balancing these posttreatment processes is essential for achieving high-efficiency and stable OSCs.

Vacuum-assisted processing techniques have emerged as a promising avenue for enhancing the performance and stability of OSCs. These techniques leverage vacuum conditions to manipulate the morphology, crystallinity, and interfacial properties of the active layer, leading to improved device performance.[31,32]

Liu et al. employed vacuum-assisted TA (VATA) to improve the morphology and crystallinity of low-bandgap perovskite films, resulting in higher efficiency and stability.[31]

Bishop et al. utilized a low vacuum to control the crystallization of spray-coated perovskite films, achieving a power conversion efficiency (PCE) of 17.8%.[33] Huang et al. also used a dynamic vacuum-assisted process to fabricate efficient and stable all-inorganic CsPbIBr2 perovskite solar cells at a low temperature of 140 °C.[34]

Lee et al. introduced the concept of vacuum deposition of an organic passivation layer on the photoactive layer to enhance efficiency, achieving a maximum PCE of 16.4%.[35] Yu et al. employed VATA for CsPbI3 films, resulting in a champion PCE of 20.06% and improved stability.[36]

Zhao et al. developed a vacuum-assisted annealing method for blade-coated polymer solar cells, demonstrating comparable performance to spin-coated devices and achieving a PCE of 10.21% in a large-area module.[32] While high vacuum can be beneficial, it can also pose challenges in terms of cost and scalability for large-scale production.[32]

In this study, we introduce a simple and accessible vacuum treatment method for the active layer of NFA BHJ OSCs. This novel approach, which we label "prevacuum," involves applying a low-pressure vacuum (−1 bar) to the deposited active layer (D18:Y6) prior to TA (see **Figure 1**). By comparing BHJ devices with and without prevacuum treatment through a series of optoelectronic characterizations and stability tests, including maximum power point (MPP) tracking and degradation rate (DR) analysis, we showcase the efficacy of this method in enhancing device stability.

2. Results and Discussion

2.1. Device Characterization

As illustrated in **Figure 2**b, the absorbance spectra of D18:Y6 active layers processed with and without prevacuum treatment. Both films exhibit a broad absorption range from 400 to 900 nm,

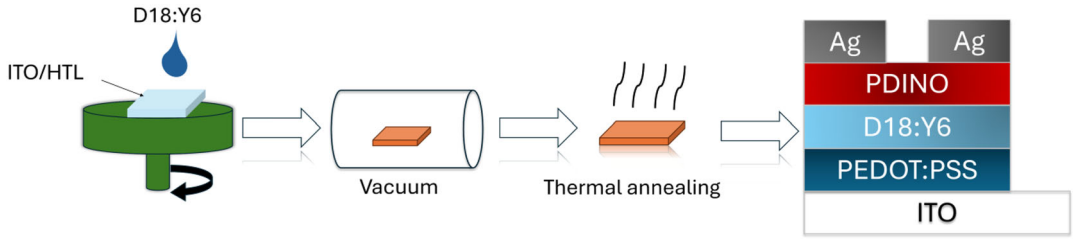

Figure 1. Schematic representation of the preparation of the active layer with vacuum treatment and the BHJ device at the end of the process.

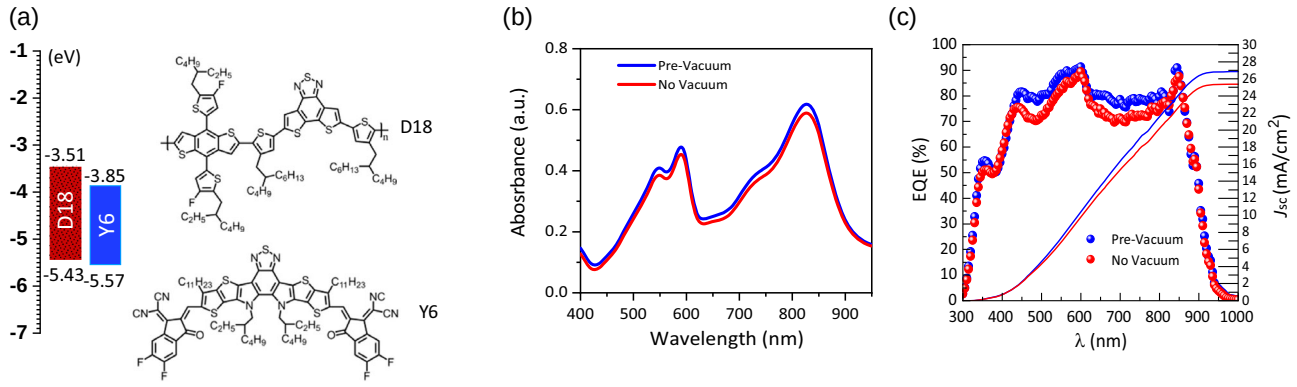

Figure 2. a) Approximate energy diagram before putting the materials in contact (left) and the D18 and Y6 chemical structures (right). The literature values used for the energy positions in the energy diagram are summarized in Table S1, Supporting Information. b) Absorption after deposition of the absorber layer on ITO. c) external quantum efficiency (EQE).

characteristic of the D18:Y6 blend. The absorption peaks between 550 and 600 nm correspond to the D18 donor, while the absorption from 750 to 900 nm is attributed to the Y6 acceptor.[37,38]

Interestingly, the prevacuum-treated active layer shows a consistently higher absorbance across the entire spectrum compared to the untreated layer. This suggests that prevacuum treatment enhances the packing density of the D18:Y6 blend, leading to improved light absorption and potentially higher charge generation in OSCs. The difference is particularly noticeable in the near-infrared region, where the Y6 acceptor is primarily responsible for light absorption.[8,39] This could imply that prevacuum treatment preferentially affects the Y6 acceptor, leading to a more favorable morphology for charge transport.

The EQE spectra of the D18:Y6 OSCs in Figure 2c show the positive impact of prevacuum treatment on device performance. The enhancement in EQE is particularly pronounced in the range of 700–900 nm, aligning with the absorption region of the Y6 acceptor. This suggests that prevacuum treatment specifically improves the charge generation and extraction efficiency within the Y6 acceptor domain. This could be attributed to the morphological changes induced by the treatment, potentially leading to better charge transport and reduced recombination within the Y6 acceptor phase. The higher EQE indicates that more photons are being converted into charge carriers and successfully extracted to the electrodes. The improved EQE translates directly to an increased short-circuit current density (J_{sc}).

To estimate the bandgap, we can analyze the onset of the EQE spectra. The onset for the prevacuum-treated device is around 907 nm, while for the nontreated device, it is slightly blueshifted to around 903 nm. Converting these wavelengths to energy using the equation $E = \frac{hc}{\lambda}$ (where h is the Planck's constant, c is the speed of light, and λ is the wavelength), we obtain approximate bandgap values of 1.36 and 1.37 eV for the prevacuum-treated and nontreated devices, respectively.[40]

This slight difference in the bandgap could be attributed to the morphological changes induced by the prevacuum treatment. The potentially enhanced molecular order resulting from the treatment might lead to a subtle narrowing of the bandgap, further contributing to the improved light absorption and charge generation observed in the prevacuum-treated device.[41–43]

Atomic force microscope (AFM) topography and 3D images of the D18:Y6 active layer have been introduced in Figure S1, Supporting Information. The prevacuum-treated device exhibits a smoother surface with a root mean square roughness of 0.940 nm, compared to 1.46 nm for the nontreated sample. A smoother interface can facilitate better charge transport, reduce trap states, and mitigate degradation pathways, ultimately leading to more efficient and longer-lasting devices.[44]

The observed enhancement in charge generation and extraction within the Y6 acceptor domain, as evidenced by the EQE spectra, can be correlated with the morphological changes induced by the prevacuum treatment. AFM images reveal a smoother and more ordered surface for the prevacuum-treated D18:Y6 blend, suggesting enhanced molecular packing and potentially larger Y6 crystalline domains. These morphological improvements facilitate efficient charge transport within the Y6 phase, leading to improved charge extraction and reduced recombination losses. This interpretation is further supported by impedance spectroscopy measurements, which show reduced charge transfer resistance in the prevacuum-treated device, particularly at lower frequencies, indicative of improved charge transport across the active layer and at the interfaces. The combination of AFM and impedance data provides strong evidence that the prevacuum treatment enhances the charge dynamics specifically within the Y6 acceptor domain, contributing to the improved device performance.

To detect the effect of the vacuum on the wettability of the active layer, the contact angle (CA) of a drop of water on the active layer (D18:Y6) has been measured and illustrated in Figure S2, Supporting Information. Table S2, Supporting Information, provides each device's CA measurement values where there is a significant difference in water CAs between prevacuum-treated (107.6°) and nontreated (97.2°) D18:Y6 active layers.

By applying vacuum, these volatile components are effectively eliminated, leaving behind a cleaner, more pristine surface. This results in a decrease in surface energy, rendering the D18:Y6 layer less attractive to water molecules. Consequently, water droplets bead up on the surface, leading to higher CAs and reduced wetting.

This enhanced hydrophobicity is crucial for mitigating the detrimental effects of PEDOT:PSS, a commonly used hole-transport layer known for its acidity and hygroscopicity. By repelling moisture, the prevacuum-treated surface minimizes water-induced degradation pathways, such as active layer deterioration, interfacial delamination, and acid-catalyzed reactions.

The current density–voltage (J–V) characteristics of the D18:Y6 OSCs with structure ITO/PEDOT:PSS/D18:Y6/PDINO/Ag, as shown in **Figure 3**a, further validate the superior performance of the prevacuum-treated device. Under 1 sun illumination, the prevacuum device exhibits a higher short-circuit current density (J_{sc}) of 26.43 mA cm^{-2} and open-circuit voltage V_{oc} of 0.82 V compared to the device without prevacuum treatment 24.72 mA cm^{-2} and V_{oc} of 0.81 V. This translates to a substantially larger fill factor (FF) of 68% and ultimately a higher maximum PCE of 14.90% prevacuum device and 13.71% for the device without prevacuum treatment. For the prevacuum devices, we performed the vacuum at varying times, and the optimum performance was achieved at 20 min, resulting in increased FF and photocurrent, as illustrated in Figure S3a and Table S3, Supporting Information. Some reported PCE% of D18:Y6 have been summarized in Table S4, Supporting Information.

We also measured dark J–V curves for the device without vacuum and for the prevacuum with different times, showing similar behavior, as depicted in Figure 3b and S3b, Supporting Information, for the optimized time. Subsequently, the dark direct current (DC) mode resistance–voltage (R–V) curves were extracted from the dark J–V characteristics (see Section S1.4 and Figure S4, Supporting Information) and an increase in the shunt resistance (R_{sh}) was observed in the prevacuum device, as illustrated in Figure S5, Supporting Information.

Figure 3c illustrates the effective voltage (V_{eff}) versus photocurrent density (J_{ph}) for both prevacuum-treated and nontreated devices. Figure S6, Supporting Information, shows the theoretical J_{ph}, J_L, and J_D as a function of voltage. The saturation current density (J_{sat}), maximum exciton generation rate (G_{max}), generation rate (G_{rat}), and exciton dissociation probabilities (P_{diss}) were calculated using the equations in Section S1.5, Supporting Information.[45,46]

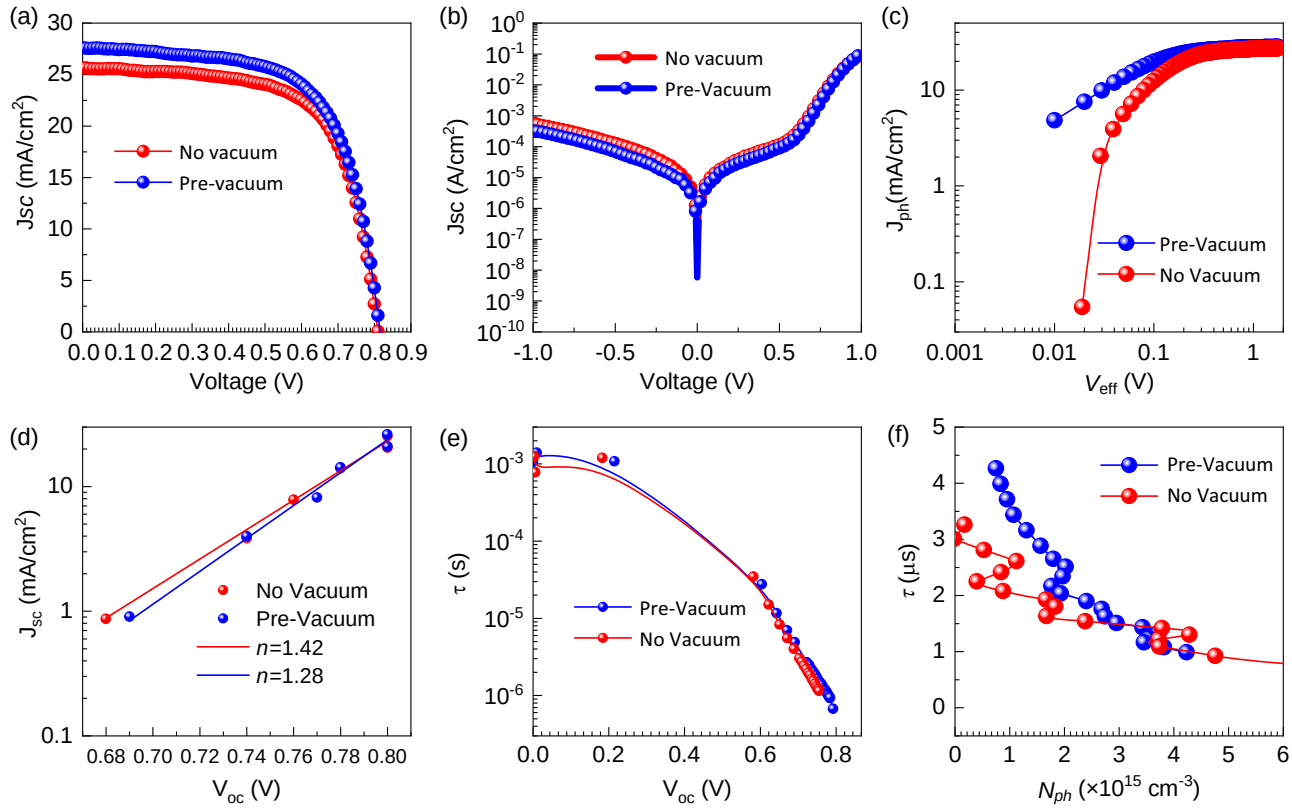

Figure 3. a) Current density–voltage measured with solar simulator, b) dark current–voltage curves, c) J_{ph} versus V_{eff}, d) short-circuit current versus open-circuit current for different illumination conditions; transient and spectroscopic characterization e) recombination lifetime as a function of open-circuit voltage, and f) photogenerated charge carriers for several illumination intensities.

As depicted in Figure 3c, photocurrent exhibits a linear increase until V_{eff} reaches 0.19 V for the prevacuum device and 0.31 V for the nontreated device. Beyond these voltages, the photocurrent largely saturates. This suggests efficient charge carrier separation at lower effective voltages for the prevacuum-treated device.[47]

Table S5, Supporting Information, summarizes the results of these measurements and calculations from the J_{ph}–V_{eff} curves. Notably, the prevacuum-treated device demonstrates a higher saturation current density J_{sat} of 27.7 mA cm^{-2} compared to 26.94 mA cm^{-2} for the nontreated device. Additionally, it boasts a higher maximum power generation rate G_{max} of 7.76×10^{25} and generation rate G_{rat} of 7.27×10^{27}, surpassing the nontreated device's G_{max} of 7.46×10^{25} and G_{rat} of 7.13×10^{27}. These findings collectively indicate the prevacuum-treated device superior capability to convert light into electrical power.[45,48,49]

Furthermore, the prevacuum-treated device exhibits a higher dissociation probability (P_{diss}) of 99.4%, compared to 95.6% for the nontreated device. This signifies that a greater proportion of photogenerated excitons successfully dissociate into free charge carriers at the donor/acceptor interface, leading to enhanced charge collection efficiency.[49] This observation aligns with the higher short-circuit current density (J_{sc}) observed for the prevacuum-treated device, as detailed in Table S2, Supporting Information.

Charge carrier recombination mechanisms within the OSCs were investigated by analyzing the current density–voltage (J–V) characteristics under varying light intensities (Figure 3d). The mechanisms of charge carrier recombination in the samples were examined by evaluating the ideality factor (n), a parameter that indicates whether recombination occurs through radiative or nonradiative processes. Detailed descriptions of the fundamental equations, formalisms for ideality factor analysis, and the measurement procedures employed can be found in Section S1.4, Supporting Information. The ideality factor (n) was evaluated for both the nonvacuum ($n = 1.42$) and prevacuum ($n = 1.28$) treated devices.[50]

A lower ideality factor generally indicates reduced recombination losses, which can lead to improved device performance, particularly in terms of FF and V_{oc}. The prevacuum treatment induced a notable reduction in the ideality factor, suggesting a suppression of trap-mediated surface recombination. This aligns with the observed increase in FF for the prevacuum-treated device. Moreover, the consistent enhancement in current density across all light intensities for the prevacuum-treated device points toward improved charge transport and/or collection efficiency, likely attributable to the vacuum-induced reduction in interfacial defects and traps.

Transient photovoltage (TPV) measurements under single illumination intensity revealed monoexponential decays

(Figure S7, Supporting Information), with representative transients depicted in Figure 3d,e. The extracted recombination lifetimes (τ) as a function of open-circuit voltage (V_{oc}) showed a subtle increase for the prevacuum-treated device at low voltages ($V_{oc} < 0.35$ V) (Figure 3e). To further elucidate this behavior, photoinduced charge extraction experiments were conducted to quantify the photogenerated charge carrier density (N_{ph}) as a function of V_{oc} (Figure S8, Supporting Information). The resulting correlation between recombination lifetime (from TPV) and photogenerated charge carrier density is illustrated in Figure 3d, revealing a distinct difference: the prevacuum-treated sample consistently exhibits higher lifetimes compared to the device without vacuum treatment.

2.2. Stability Study

To provide a comprehensive assessment of the stability of the fabricated OSCs, we conducted a series of stability tests under various conditions, as summarized in Table S6, Supporting Information. These tests included MPP tracking, open-circuit conditions, and light soaking under 1 sun illumination. The results of these tests were then compared to previously reported stability data for D18:Y6 devices under different conditions, as presented in Table S7, Supporting Information. This comparative analysis allows us to evaluate the effectiveness of our prevacuum treatment in enhancing the long-term stability of the OSCs.

2.2.1. MPP Under Constant Illumination

In the first stability test, devices were subjected to operational conditions simulating real-world use: a nonisolated holder with continuous MPP tracking under 1 sun equivalent white LED illumination at 46 °C ± 3 °C with spectrum shown in Figure S9, Supporting Information. **Figure 4**a displays the normalized MPP results over time, revealing a striking difference in performance (see workflow chart in Figure S10a, Supporting Information).

The device with direct TA (no vacuum) of the D18:Y6 blend experienced a rapid decline, losing 30% of its initial power within a mere 4.5 h. In contrast, the device incorporating prevacuum treatment demonstrated superior stability, with a 30% power loss occurring over a significantly extended period of 8.25 h.

This notable difference in MPP DRs underscores the crucial role of prevacuum treatment in enhancing device stability under operational conditions. This finding suggests that prevacuum treatment may be a key factor in the development of more durable and long-lasting OSCs.

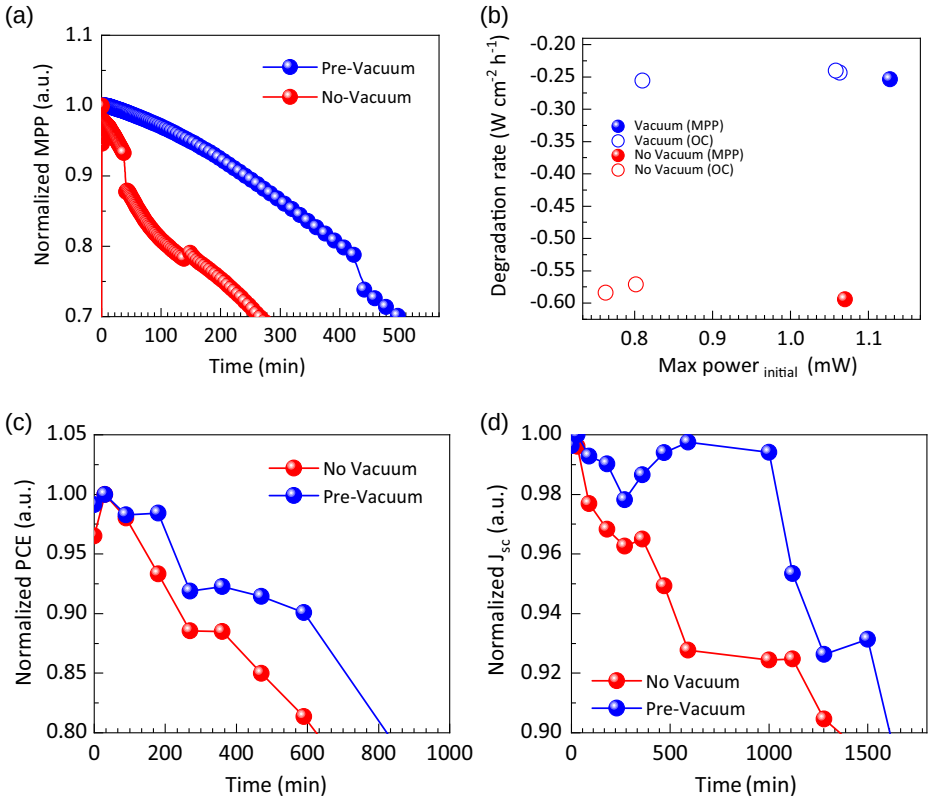

Figure 4. Device stability tests considering a) operation under room conditions with MPP tracking under continuous 1 sun illumination (LED equivalent). b) DR versus the initial PCE. Device stability tests considering light soaking under room conditions with standard 1 sun illumination (solar simulator). c) Normalized PCE versus time. d) Normalized J_{sc} versus time.

2.2.2. Open-Circuit Conditions Under Constant Illumination

In contrast to MPP tracking under illumination, which involves all operational parameters, evaluating photostability can be isolated by setting the device in open-circuit condition, where no current flows. This minimizes overheating from current dissipation and other degradation mechanisms linked to external voltage bias.

The remaining disconnected pixels/diodes from MPP tracking on the substrate were concurrently subjected to a light stability test under open-circuit conditions during each operational stability test (see workflow chart in Figure S10b, Supporting Information). This dual-test approach provides valuable insights into both the operational and inherent photostability of the devices.

Stability test results can be further analyzed using DRs, offering a quantitative measure of performance decline over time. A dynamic, time-dependent DR can be calculated by $\left(\mathrm{DR} = \frac{X_{\mathrm{final}} - X_{\mathrm{initial}}}{t_{\mathrm{st}}}\right)$ of the performance parameter X which could be PCE or power and t_{st} is the stability test of duration.

Figure 4b shows the DR versus the initial maximum power values where the T80 is used from the MPP tracking operational test as the reference point for degradation assessment.

We can observe the nearly identical DR values for prevacuum diodes in both MPP and open-circuit (OC) light tests, whereas no vacuum cells exhibit slightly larger difference in DR under OC conditions. This suggests that vacuum treatment may effectively inhibit reactive pathways that are typically triggered during OC, when no current flows through the cell. This finding highlights a potential advantage of vacuum treatment in enhancing the long-term stability of OSCs under various operating conditions.

2.2.3. Light Soaking Under 1 Sun Solar Simulator

Figure 4c,d illustrates the impact of vacuum treatment on the stability of OSCs under continuous 1 sun illumination (see workflow chart in Figure S10c, Supporting Information). Figure 4c shows the normalized PCE over time, while Figure 4d depicts the normalized J_{sc}. In both cases, the prevacuum-treated devices exhibit superior stability compared to the no-vacuum devices.

The prevacuum-treated cells maintain a higher PCE and J_{sc} throughout the duration of the experiment, indicating a slower DR. The device with direct TA (no vacuum) of the D18:Y6 blend lost 20% of its initial PCE within 630 min (10.5) hours. In contrast, the device incorporating prevacuum treatment demonstrated superior stability, with a 20% PCE loss occurring over a significantly extended period of 830 min (13.8) hours.

This enhanced stability is likely attributed to the removal of impurities and trapped air/moisture within the active layer during the vacuum treatment process. These contaminants can lead to detrimental reactions and morphological changes, accelerating the degradation of the solar cell performance.[51] By mitigating these effects, vacuum treatment significantly improves the operational lifetime and overall stability of OSCs under light soaking conditions.

The stability observed in MPP tracking can be attributed to the separation of donor and acceptor domains within the material. This phase separation promotes the collection of charge carriers at the electrodes in the case of prevacuum active layer.[52]

The higher CA of water on the prevacuum-treated device suggests a more hydrophobic surface, which can reduce the penetration of moisture and subsequent degradation of the organic materials.

In addition, the lower surface roughness of the prevacuum-treated device, as evidenced by AFM measurements, could lead to better interfacial contact between the active layer and the electrodes, minimizing charge recombination losses.

These highlight the impact of the vacuum treatment in improving surface hydrophobicity and reducing surface roughness; vacuum treatment can significantly enhance the stability of these devices, paving the way for their widespread adoption as a sustainable energy source.

The Nyquist and Bode plots under 1 sun illumination reveal distinct differences in the impedance characteristics of prevacuum-treated and nontreated devices, both in fresh state T100 and at T80 (80% of initial PCE) as illustrated in **Figure 5**a–d and S11, Supporting Information. The fresh prevacuum-treated device exhibits a smaller semicircle in the Nyquist plot and a lower frequency peak in the Bode plot compared to the nontreated device. This indicates lower charge transfer resistance and faster charge extraction processes,[53] suggesting that the vacuum process improves the interface quality between the active layer (D18:Y6) and the charge transport layers.

At T80, the prevacuum-treated device maintains a relatively stable impedance response, with only a minor increase in the semicircle size and a slight shift in the frequency peak. In contrast, the nontreated device shows a significant increase in charge transfer resistance and a substantial shift toward lower frequencies, signifying a more pronounced degradation of the active layer and interfaces. The experimental data have been fitted by an equivalent electrical model using three resistor/capacitor (3RC) model as shown in Figure S12, Supporting Information, and the extracted fitted parameters are summarized in Table S8, Supporting Information.[54]

This disparity in degradation behavior can be attributed to the effects of the vacuum process on the D18:Y6 active layer. The vacuum treatment likely removes trapped solvent molecules and impurities, leading to a denser and more homogenous film morphology. This improved morphology could result in better charge transport, reduced recombination losses, and enhanced resistance to degradation under operational stress. Additionally, the vacuum process might also promote better interfacial contact between the active layer and the transport layers, further contributing to the observed stability enhancement.

Figure 5e shows the DC conductivity derived from Nyquist plots of the deposited active layer D18:Y6. The prevacuum-treated device exhibits higher conductivity across all frequencies compared to the nontreated device, suggesting improved charge transport properties within the active layer due to the removal of impurities and enhanced molecular packing during the vacuum process. At T80, the prevacuum-treated device maintains a higher conductivity, while the nontreated device shows a more pronounced decline, indicating superior stability in the former.

The photoluminescence (PL) spectra are illustrated in Figure 5f. The fresh nontreated device exhibits a slightly stronger

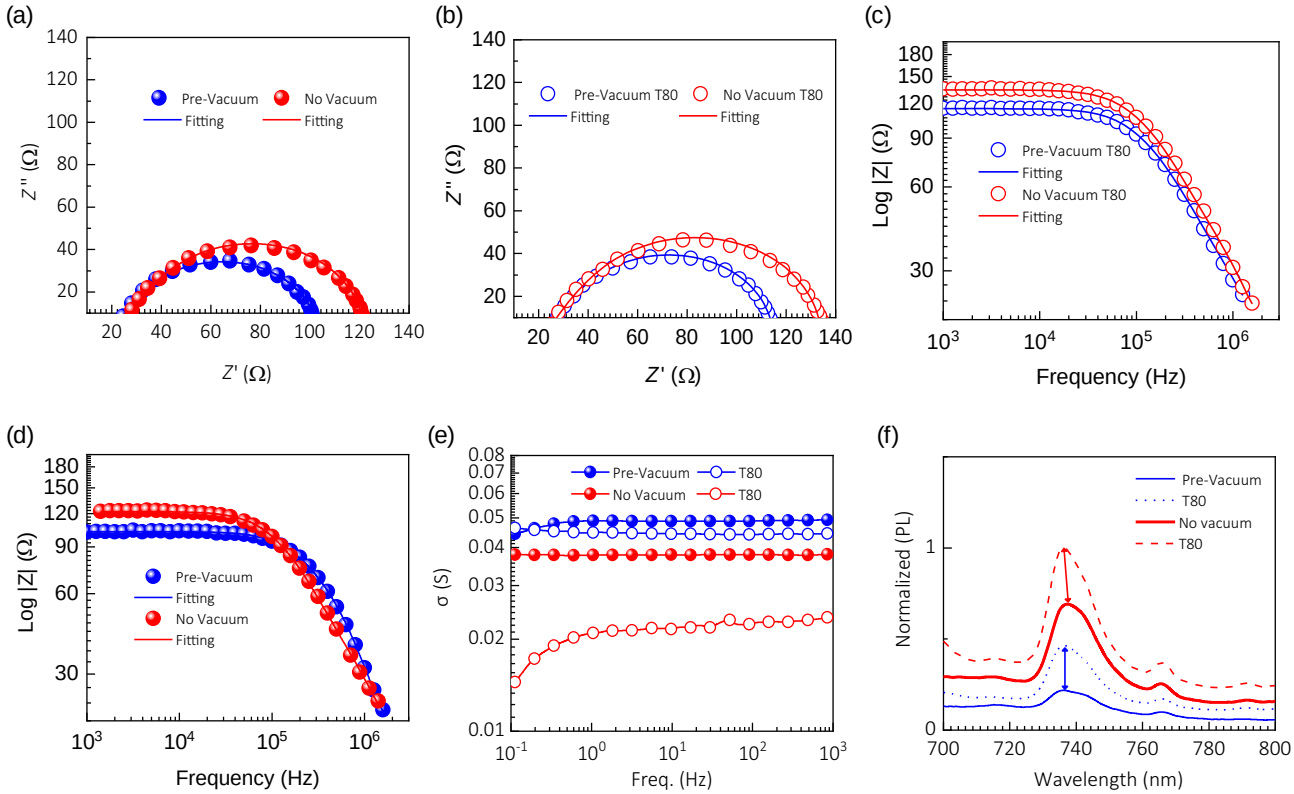

Figure 5. Nyquist plot representation at open-circuit for a single illumination intensity a) T100 of PCE and b) T80 of PCE. Magnitude of the real and imaginary parts for the devices c) T100 of PCE and d) T80 of PCE. e) Surface conductivity versus frequency for the different absorption layers and f) PL spectra.

PL intensity compared to the prevacuum-treated one, signifying that more excitons recombine radiatively in the nontreated device, likely due to increased trap states or less efficient charge extraction. At T80, the PL intensity for both devices is increased, but the increase is more pronounced for the nontreated device, suggesting that vacuum treatment mitigates degradation-induced recombination centers.

The vacuum process significantly influences both the charge transport and recombination dynamics in D18:Y6 active layers. The enhanced conductivity and reduced PL intensity in prevacuum-treated devices translate to superior charge extraction and reduced recombination losses, which contribute to improved device performance and stability. The preservation of these properties at T80 highlights the crucial role of vacuum treatment in mitigating degradation pathways and ensuring the long-term operational stability of OSCs.

The core mechanism of the prevacuum treatment lies in the removal of volatile components and impurities from the active layer before TA. This process leads to several beneficial outcomes that are likely improved morphology and reducing degradation to be relevant in various BHJ systems.[26,55]

3. Conclusions

In conclusion, this study introduces a novel prevacuum treatment method for D18:Y6 NFA BHJ OSCs, demonstrating significant enhancement in device stability under various operational conditions. The application of a low-pressure vacuum prior to TA resulted in a modest improved PCE, attributed to enhanced light absorption, charge generation, extraction, and reduced recombination losses. These improvements are correlated with the enhanced interfacial contact facilitated by the vacuum process. The application of a low-pressure vacuum prior to TA resulted in significantly enhanced device long-term stability under MPP tracking, open-circuit conditions, and light soaking. This enhancement is attributed to the removal of impurities and trapped solvent molecules, leading to improved film morphology, reduced recombination losses, and better interfacial contact. The promising results obtained with the D18:Y6 system suggest that the prevacuum treatment could be a valuable strategy for enhancing the performance and stability of other BHJ OSCs. This straightforward and accessible technique represents a step forward in the development of efficient and durable OSCs for practical applications.

4. Experimental Section

Device Fabrication: The indium tin oxide (ITO) substrates were first cleaned in a detergent and water bath using ultrasonic agitation. This was followed by a 10 min ultrasonic cleaning cycle in ethanol, methanol, and isopropanol, sequentially. After cleaning, the ITOs were baked in an oven at 100 °C for 10 min. Finally, the samples were treated with UV

(UV–ozone) for 15 min to remove any remaining organic contaminants and activate the surface.

The PEDOT:PSS aqueous solution was filtered through a 0.20 μm PFTE filter and then spin-coated onto the precleaned ITO substrates. The resulting PEDOT:PSS film was annealed in air at 150 °C for 20 min.[45]

A 10 mg mL^{-1} blend solution of D18 donor and Y6 acceptor (1:1.6 ratio) in chloroform was prepared by stirring at 70 °C for 2 h. This solution was then spin-coated onto the HTL at 2000 rpm for 40 s using dynamic deposition. The resulting film was thermally treated at 100 °C, with or without a prior 15 min vacuum treatment at −1 bar.

A 1.5 mg mL^{-1} PDINO solution in methanol was prepared, filtered, and spin-coated at 3000 rpm for 30 s. A 100 nm Ag film was then thermally evaporated onto the PDINO layer under high vacuum 1×10^{-6} mbar, utilizing a shadow mask to define the active device area of 0.09 cm^2.

Vacuum Technique: Vacuum Chamber Setup and Specific Pressure: The prevacuum treatment was performed using antechamber vacuum that attached to the glove box capable of reaching low pressure. The active layer films were placed inside the chamber in uncovered holder.

The pressure inside the vacuum chamber was maintained at −1 bar during the prevacuum treatment.

Material Characterization: Comprehensive details regarding the purchasing, preparation, and characterization of the materials employed in this study are provided in Section S1, Supporting Information.

Supporting Information

Supporting Information is available from the Wiley Online Library or from the author.

Acknowledgements

M.S. acknowledges the financial support from Programa Martí i Franquès. This work was further supported by the Spanish Ministerio de Ciencia e Innovación (MICINN/FEDER) under Grants PDI2021-128342OB-I00, by the Agency for Management of University and Research Grants (AGAUR) ref 2021-SGR-00739, and from the Catalan Institution for Research and Advanced Studies (ICREA) under the ICREA Academia Award. O.A. acknowledges the Juan de la Cierva Fellowship grant FJC2021-046887-I funded by MICIU/AEI/10.13039/501100011033 and by the European Union NextGenerationEU/PRTR.

Conflict of Interest

The authors declare no conflict of interest.

Author Contributions

Mohamed Samir: Data curation (equal); Formal analysis (equal); Investigation (equal); Methodology (equal); Validation (equal); Visualization (lead); Writing—original draft (lead). **Angel Sacramento**: Formal analysis (equal); Investigation (equal); Methodology (equal); Writing—review & editing (equal). **Osbel Almora**: Conceptualization (equal); Data curation (equal); Formal analysis (equal); Investigation (equal); Methodology (equal); Supervision (equal); Validation (equal); Writing—review & editing (equal). **Josep Pallarès**: Formal analysis (equal); Investigation (equal); Supervision (equal); Validation (equal); Writing—review & editing (equal). **Lluis F. Marsal**: Conceptualization (lead); Formal analysis (equal); Funding acquisition (lead); Investigation (equal); Project administration (lead); Supervision (lead); Validation (equal); Writing—review & editing (equal).

Data Availability Statement

The data that support the findings of this study are available from the corresponding author upon reasonable request.

Keywords

charge transport, device stability, morphology control, nonfullerene acceptors, optoelectronic characterization, organic photovoltaics, vacuum-assisted

Received: July 2, 2024
Revised: August 20, 2024
Published online: September 13, 2024

[1] Y. Liu, B. Liu, C.-Q. Ma, F. Huang, G. Feng, H. Chen, J. Hou, L. Yan, Q. Wei, Q. Luo, Q. Bao, W. Ma, W. Liu, W. Li, X. Wan, X. Hu, Y. Han, Y. Li, Y. Zhou, Y. Zou, Y. Chen, Y. Li, Y. Chen, Z. Tang, Z. Hu, Z.-G. Zhang, Z. Bo, *Sci. China Chem.* **2022**, *65*, 224.
[2] F. Zhao, H. Zhang, R. Zhang, J. Yuan, D. He, Y. Zou, F. Gao, *Adv. Energy Mater.* **2020**, *10*, 2002746.
[3] A. Armin, W. Li, O. J. Sandberg, Z. Xiao, L. Ding, J. Nelson, D. Neher, K. Vandewal, S. Shoaee, T. Wang, H. Ade, T. Heumüller, C. Brabec, P. Meredith, *Adv. Energy Mater.* **2021**, *11*, 2003570.
[4] O. Almora, C. I. Cabrera, S. Erten-Ela, K. Forberich, K. Fukuda, F. Guo, J. Hauch, A. W. Y. Ho-Baillie, T. J. Jacobsson, R. A. J. Janssen, T. Kirchartz, M. A. Loi, X. Mathew, D. B. Mitzi, M. K. Nazeeruddin, U. W. Paetzold, B. P. Rand, U. Rau, T. Someya, E. Unger, L. Vaillant-Roca, C. J. Brabec, *Adv. Energy Mater.* **2024**, *14*, 2303173.
[5] K. S. Ram, J. Singh, *Adv. Theor. Simul.* **2020**, *3*, 2000047.
[6] H. Yao, J. Hou, *Angew. Chem., Int. Ed.* **2022**, *61*, e202209021.
[7] D. Luo, W. Jang, D. D. Babu, M. S. Kim, D. H. Wang, A. K. K. Kyaw, *J. Mater. Chem. A* **2022**, *10*, 3255.
[8] H. Gao, Y. Sun, L. Meng, C. Han, X. Wan, Y. Chen, *Small* **2023**, *19*, 2205594.
[9] K. Fukuda, K. Yu, T. Someya, *Adv. Energy Mater.* **2020**, *10*, 2000765.
[10] W. B. Tarique, A. Uddin, *Mater. Sci. Semicond. Process.* **2023**, *163*, 107541.
[11] J. Jin, Q. Wang, K. Ma, W. Shen, L. A. Belfiore, X. Bao, J. Tang, *Adv. Funct. Mater.* **2023**, *33*, 2213324.
[12] Y. Li, W. Huang, D. Zhao, L. Wang, Z. Jiao, Q. Huang, P. Wang, M. Sun, G. Yuan, *Molecules* **2022**, Vol. *27*, 1800.
[13] P. Ding, D. Yang, S. Yang, Z. Ge, *Chem. Soc. Rev.* **2024**, *53*, 2350.
[14] M. Wu, B. Ma, S. Li, J. Han, W. Zhao, *Adv. Funct. Mater.* **2023**, *33*, 2305445.
[15] G. Dennler, M. C. Scharber, C. J. Brabec, *Adv. Mater.* **2009**, *21*, 1323.
[16] A. A. A. Torimtubun, M. Méndez, E. Moustafa, J. Pallarès, E. Palomares, L. F. Marsal, *Sol. RRL* **2023**, *7*, 2300228.
[17] D. He, F. Zhao, C. Wang, Y. Lin, *Adv. Funct. Mater.* **2022**, *32*, 2111855.
[18] L. Duan, A. Uddin, *Adv. Sci.* **2020**, *7*, 1903259.
[19] J. Huang, H. Wang, K. Yan, X. Zhang, H. Chen, C.-Z. Li, J. Yu, *Adv. Mater.* **2017**, *29*, 1606729.
[20] X. Xu, L. Yu, H. Meng, L. Dai, H. Yan, R. Li, Q. Peng, *Adv. Funct. Mater.* **2022**, *32*, 2108797.
[21] Y. Lin, Y. Firdaus, M. I. Nugraha, F. Liu, S. Karuthedath, A.-H. Emwas, W. Zhang, A. Seitkhan, M. Neophytou, H. Faber, E. Yengel, I. McCulloch, L. Tsetseris, F. Laquai, T. D. Anthopoulos, *Adv. Sci.* **2020**, *7*, 1903419.
[22] S. Rafique, S. M. Abdullah, K. Sulaiman, M. Iwamoto, *Renewable Sustainable Energy Rev.* **2018**, *84*, 43.

[23] Y. Zhang, K. Liu, J. Huang, X. Xia, J. Cao, G. Zhao, P. W. K. Fong, Y. Zhu, F. Yan, Y. Yang, X. Lu, G. Li, *Nat. Commun.* **2021**, *12*, 4815.
[24] S. Mahdy, M. Feteha, M. Soliman, H. Hussien, T. Sadat-Shafai, S. Ebrahim, *J. Mater. Sci.* **2023**, *58*, 17543.
[25] Q. An, X. Ma, J. Gao, F. Zhang, *Sci. Bull.* **2019**, *64*, 504.
[26] C. McDowell, M. Abdelsamie, M. F. Toney, G. C. Bazan, *Adv. Mater.* **2018**, *30*, 1707114.
[27] M. Babics, R.-Z. Liang, K. Wang, F. Cruciani, Z. Kan, M. Wohlfahrt, M.-C. Tang, F. Laquai, P. M. Beaujuge, *Chem. Mater.* **2018**, *30*, 789.
[28] S. Bao, H. Yang, H. Fan, J. Zhang, Z. Wei, C. Cui, Y. Li, *Adv. Mater.* **2021**, *33*, 2105301.
[29] M. Jiang, H.-R. Bai, H.-F. Zhi, J.-K. Sun, J.-L. Wang, F. Zhang, Q. An, *ACS Energy Lett.* **2021**, *6*, 2898.
[30] E. Moustafa, L. F. Marsal, J. Pallarès, *ACS Appl. Energy Mater.* **2022**, *5*, 4390.
[31] M. Liu, Z. Chen, Q. Xue, S. H. Cheung, S. K. So, H.-L. Yip, Y. Cao, *J. Mater. Chem. A* **2018**, *6*, 16347.
[32] W. Zhao, Y. Zhang, S. Zhang, S. Li, C. He, J. Hou, *J. Mater. Chem. C* **2019**, *7*, 3206.
[33] J. E. Bishop, J. A. Smith, C. Greenland, V. Kumar, N. Vaenas, O. S. Game, T. J. Routledge, M. Wong-Stringer, C. Rodenburg, D. G. Lidzey, *ACS Appl. Mater. Interfaces* **2018**, *10*, 39428.
[34] J. Huang, S. He, W. Zhang, A. Saparbaev, Y. Wang, Y. Gao, L. Shang, G. Dong, L. Nurumbetova, G. Yue, Y. Tu, *Sol. RRL* **2022**, *6*, 2100839.
[35] B. Lee, S. Jeong, Y. Cho, M. Jeong, S. M. Lee, J. Oh, C. Yang, *Adv. Funct. Mater.* **2020**, *30*, 2005037.
[36] G. Yu, K.-J. Jiang, W.-M. Gu, Y. Li, Y. Lin, Y. Xu, X. Jiao, T. Xue, Y. Zhang, Y. Song, *Angew. Chem., Int. Ed.* **2022**, *61*, e202203778.
[37] S. Liu, Y. Zhou, Z. Liang, B. Zhao, W. Wang, Z. Xue, K. Ding, Z. Cong, H. Wu, G. Lu, C. Gao, *ACS Appl. Energy Mater.* **2023**, *6*, 5047.
[38] A. Zeng, X. Ma, M. Pan, Y. Chen, R. Ma, H. Zhao, J. Zhang, H. K. Kim, A. Shang, S. Luo, I. C. Angunawela, Y. Chang, Z. Qi, H. Sun, J. Y. L. Lai, H. Ade, W. Ma, F. Zhang, H. Yan, *Adv. Funct. Mater.* **2021**, *31*, 2102413.
[39] L. Chen, R. Ma, J. Yi, T. A. Dela Peña, H. Li, Q. Wei, C. Yan, J. Wu, M. Li, P. Cheng, H. Yan, G. Zhang, G. Li, *Aggregate* **2024**, *5*, e455.
[40] O. Almora, C. I. Cabrera, J. Garcia-Cerrillo, T. Kirchartz, U. Rau, C. J. Brabec, *Adv. Energy Mater.* **2021**, *11*, 2100022.
[41] D. E. Motaung, G. F. Malgas, S. S. Nkosi, G. H. Mhlongo, B. W. Mwakikunga, T. Malwela, C. J. Arendse, T. F. G. Muller, F. R. Cummings, *J. Mater. Sci.* **2013**, *48*, 1763.
[42] Y. Xie, C. Zhou, X. Ma, S. Y. Jeong, H. Y. Woo, F. Huang, Y. Yang, H. Yu, J. Li, F. Zhang, K. Wang, X. Zhu, *Adv. Energy Mater.* **2024**, *14*, 2400013.
[43] D. Zhang, P. Fan, J. Shi, Y. Zheng, J. Zhong, J. Yu, *Nano Res.* **2021**, *14*, 1319.
[44] M. Samir, E. Moustafa, O. Almora, M. Ramírez-Como, M. P. Montero-Rama, J. G. Sánchez, E. Palomares, J. Pallarès, L. F. Marsal, *ACS Appl. Mater. Interfaces* **2024**, *16*, 16317.
[45] E. Moustafa, M. Méndez, J. G. Sánchez, J. Pallarès, E. Palomares, L. F. Marsal, *Adv. Energy Mater.* **2023**, *13*, 2203241.
[46] E. Moustafa, A. A. A. Torimtubun, J. Pallarès, L. F. Marsal, *Sol. RRL* **2022**, *6*, 2100480.
[47] E. Moustafa, M. Méndez, J. Pallarès, L. F. Marsal, *Sol. Energy Mater. Sol. Cells* **2022**, *248*, 111985.
[48] B.-H. Jiang, Y.-P. Wang, C.-Y. Liao, Y.-M. Chang, Y.-W. Su, R.-J. Jeng, C.-P. Chen, *ACS Appl. Mater. Interfaces* **2021**, *13*, 1076.
[49] Z. Liu, N. Wang, *J. Mater. Chem. C* **2019**, *7*, 10039.
[50] O. Almora, K. T. Cho, S. Aghazada, I. Zimmermann, G. J. Matt, C. J. Brabec, M. K. Nazeeruddin, G. Garcia-Belmonte, *Nano Energy* **2018**, *48*, 63.
[51] M. Ramírez-Como, E. Moustafa, M. Samir, A. A. A. Torimtubun, J. G. Sánchez, J. Pallarès, L. F. Marsal, *Sustainable Energy Fuels* **2023**, *7*, 3883.
[52] A. Sacramento, M. Ramírez-Como, V. S. Balderrama, J. G. Sánchez, J. Pallarès, L. F. Marsal, M. Estrada, *J. Mater. Chem. C* **2021**, *9*, 6518.
[53] A. Sacramento, J. L. Abad, M. Ramírez-Como, V. S. Balderrama, M. Estrada, *Sustainable Energy Fuels* **2024**, *8*, 103.
[54] A. C. Lazanas, M. I. Prodromidis, *ACS Meas. Sci. Au* **2023**, *3*, 162.
[55] F. Zhao, C. Wang, X. Zhan, *Adv. Energy Mater.* **2018**, *8*, 1703147.